Three-dimensional microscopy of the tumor microenvironment *in vivo* using optical frequency domain imaging

Benjamin J Vakoc*, Ryan M Lanning*, James A Tyrrell, Timothy P Padera, Lisa A Bartlett, Triantafyllos Stylianopoulos, Lance L Munn, Guillermo J Tearney, Dai Fukumura, Rakesh K Jain†, and Brett E Bouma†

*Authors contributed equally to this work
†Authors to whom correspondence should be addressed: R.K.J (jain@steele.mgh.harvard.edu) or B.E.B (bouma@helix.mgh.harvard.edu)

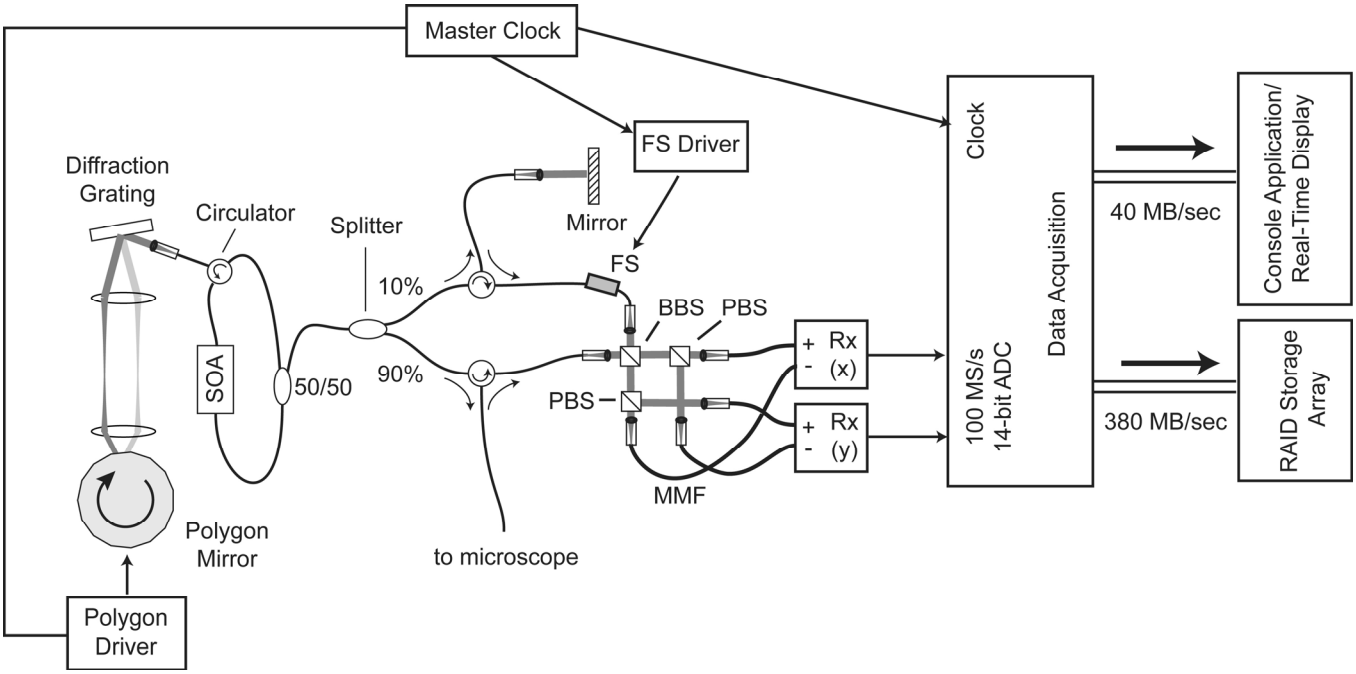

Supplementary Figure 1. OFDI instrumentation. The optical frequency domain imaging system uses a swept-wavelength laser source comprising a semiconductor optical amplifier (SOA) as the gain element inside a fiber ring cavity. The swept filter is based on a polygon mirror (Lincoln Laser). The laser output is split by a 10%/90% coupler to the reference arm/sample arm. The sample arm light is directed to the microscope with an optical circulator (), while the reference arm light is directed to a fixed reflector. An acousto-optic frequency shifter (FS) at 25 MHz offsets to coherence range from DC. A free-space polarization-diverse and balanced optical demodulation circuit comprising broadband beam splitters (BBS) and polarization beam splitters (PBS) generates four optical signals coupled to multimode fiber (MMF). These fibers relay the optical signals to two balanced receivers (Rx, New Focus), outputting two electrical signals. A two-channel 100 MS/s digitizer (Signatec) is used to acquire these signals and transfers this data directly to a RAID storage array. Approximately 10% of this data is processed in real-time on the CPU to provide image feedback. A single master clock is used to lock the polygon driver, frequency shifter, and data acquisition board to achieve high phase sensitivity.

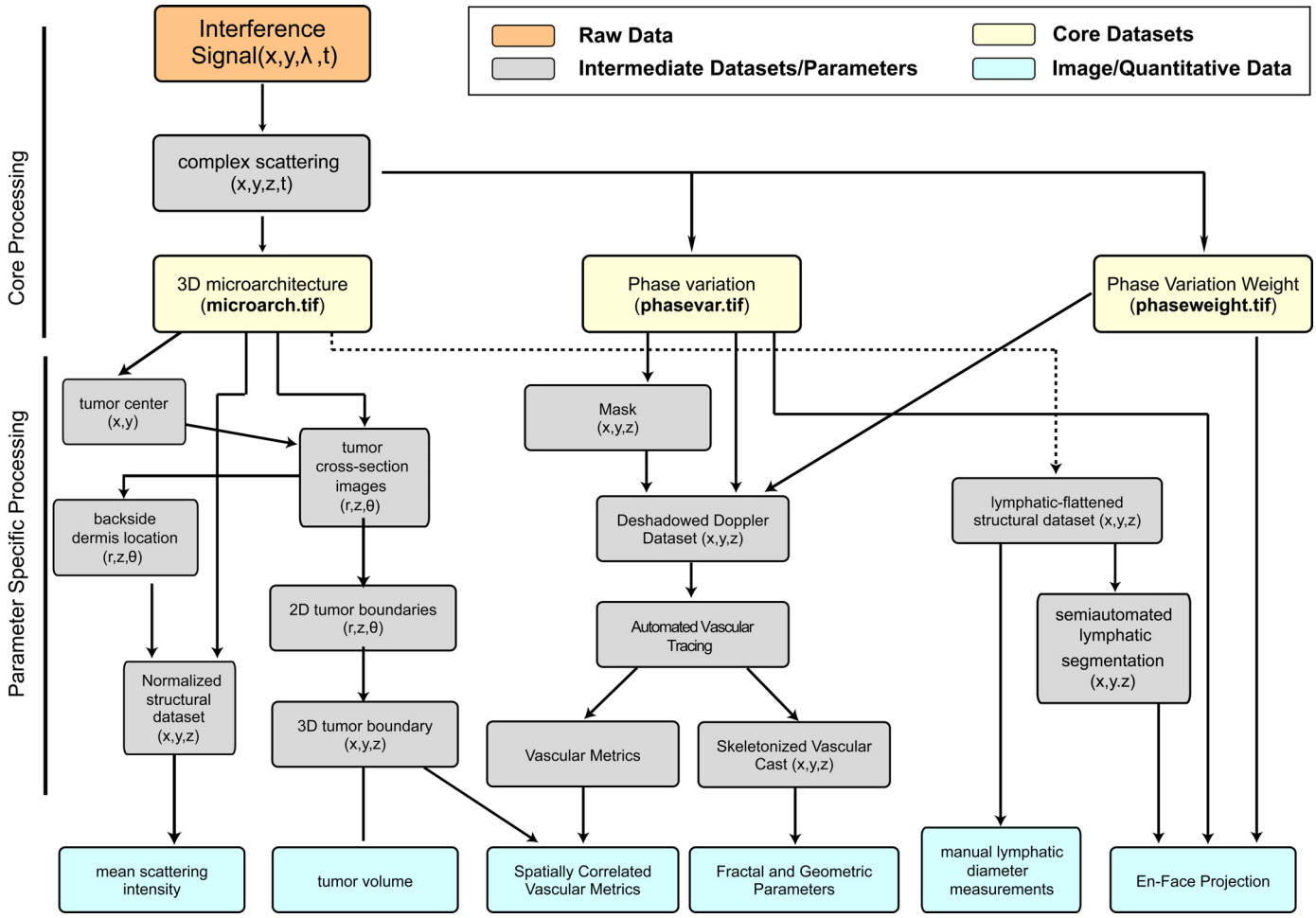

Supplementary Figure 2. Signal processing algorithms and quantitative analysis. Using the raw spatiotemporal reflectance data from OFDI, all of the angiographic, lymphangiographic and microanatomical images, as well as the biological metrics, are obtained through a series of processes represented here. Each step within the flowchart is described in detail in **Supplementary Methods.**

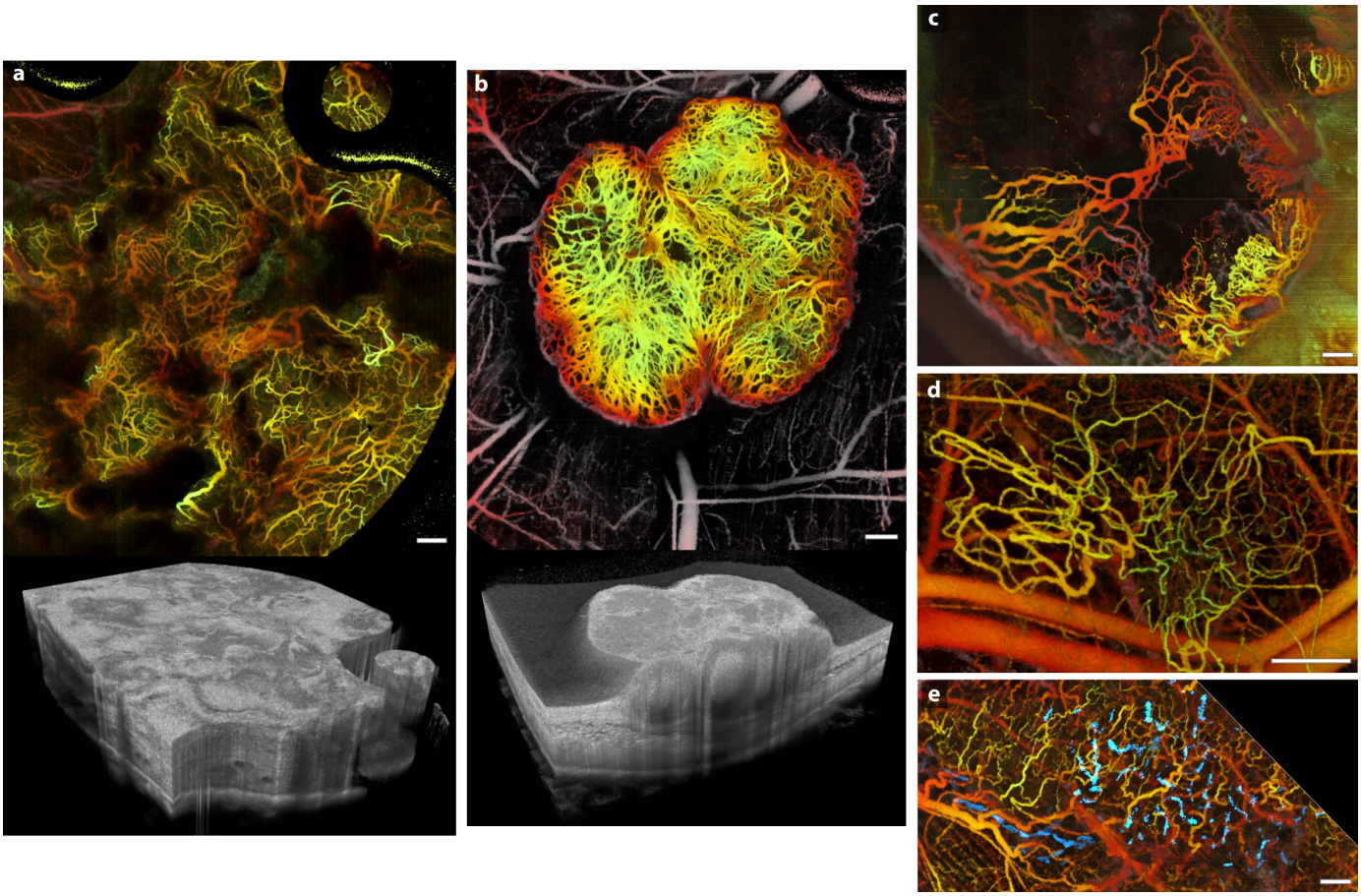

Supplementary Figure 3. OFDI angiography across tumor types and sites. (**a**) A human breast cancer cell line (MDA-MB-361HK) growing in the mammary fat pad window chamber model of a female SCID mouse. Large avascular regions are notable in the vascular image (*top*) and reflected in the topographically diffuse tumor microstructure (*bottom*). (**b**) Tumor vasculature of a human colorectal adenocarcinoma (LS174T) implanted in the dorsal skinfold chamber of a SCID mouse (*top*). Non-viable tissue is evident within the tumor nodules on cross-section (lighter regions) in the tissue scattering intensity image (*bottom*). (**c**) Angiography of a subcutaneous orthotopic human breast tumor xenograft (MDA-MD-231BR) imaged by the skin flap preparation. (**d**) Limited vasculature of the human soft-tissue sarcoma (HSTS-26T) growing orthotopically in the dorsal skinfold chamber. (**e**) Simultaneous vascular and lymphatic imaging of a tumor and nearby normal tissue in the ear of a nude mouse, a commonly utilized model in the study of tumor-associated lymphatics. Scale bars, 500 μm.

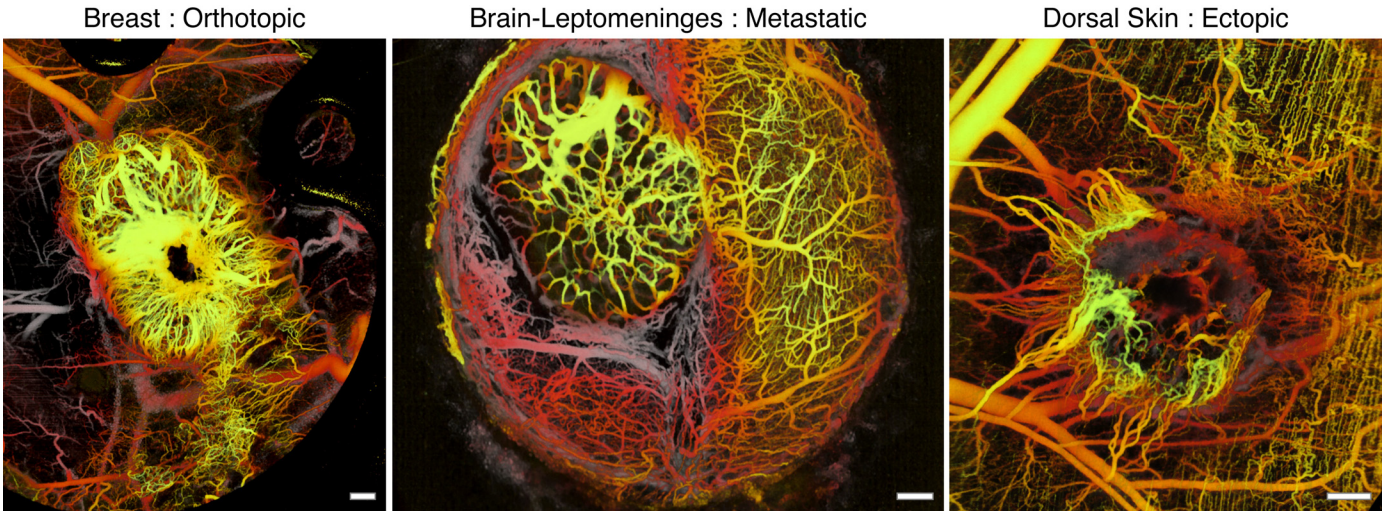

Supplementary Figure 4. Imaging across tissue microenvironments reveals strikingly different vascular networks. The murine mammary carcinoma is shown in three different anatomical locations representative of both primary and metastatic disease. Scale bars, 500 μm.

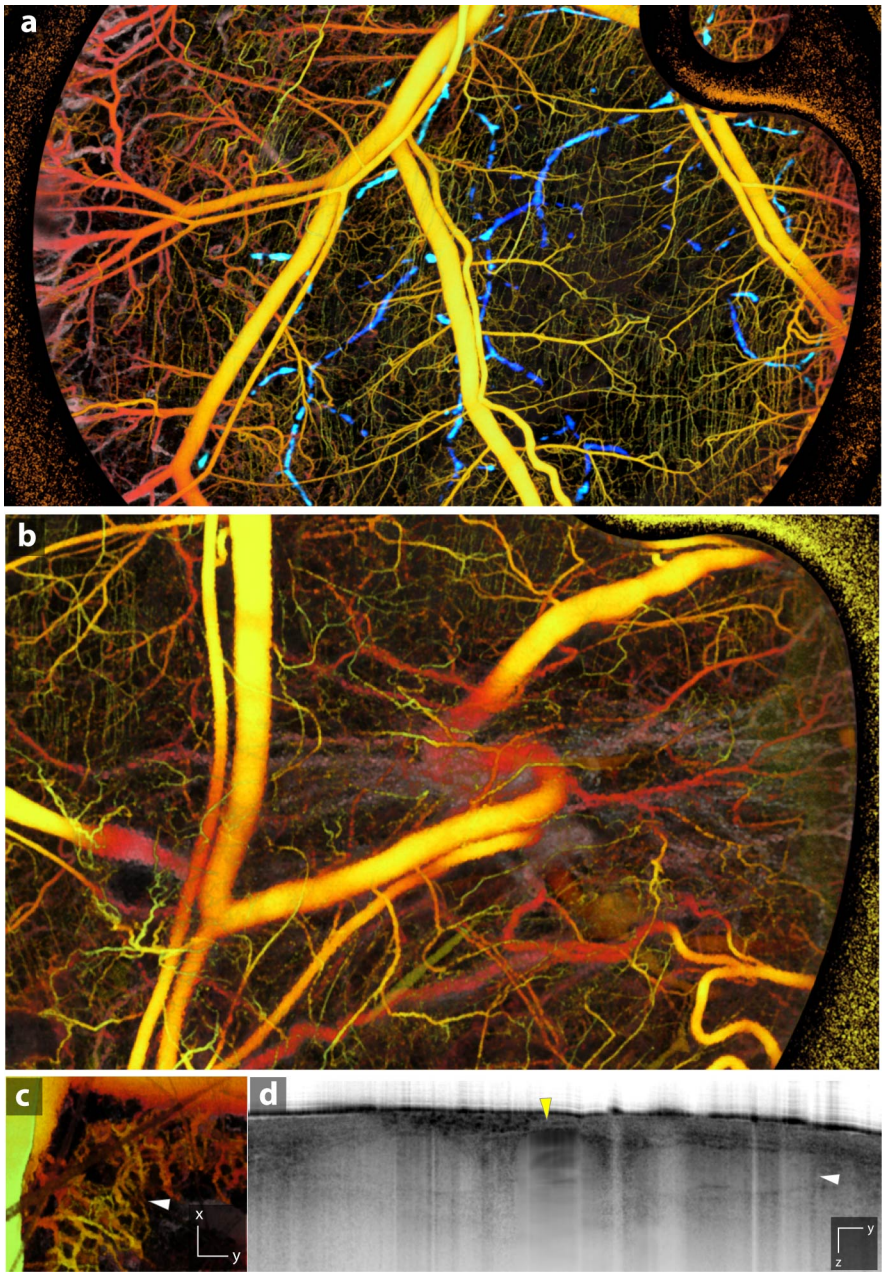

Supplementary Figure 5. OFDI angiography of normal tissues. (**a**) Vascular and lymphatic networks in normal skin within the dorsal skinfold chamber window model implanted on a SCID mouse. (**b**) Normal vasculature of the mammary fat pad window model implanted around the third mammary gland. The collection of large vessels near the center of the field are supplying the areola on the underside of the chamber. (**c**,**d**). OFDI microscopy of marrow within the mouse calvarium revealing vasculature within the marrow space (*c*) and corresponding microanatomy depicted in the cross-sectional structural image (*d*) showing marrow regions (white arrowhead, ▻) and the central sinus (yellow arrowhead, ▻).

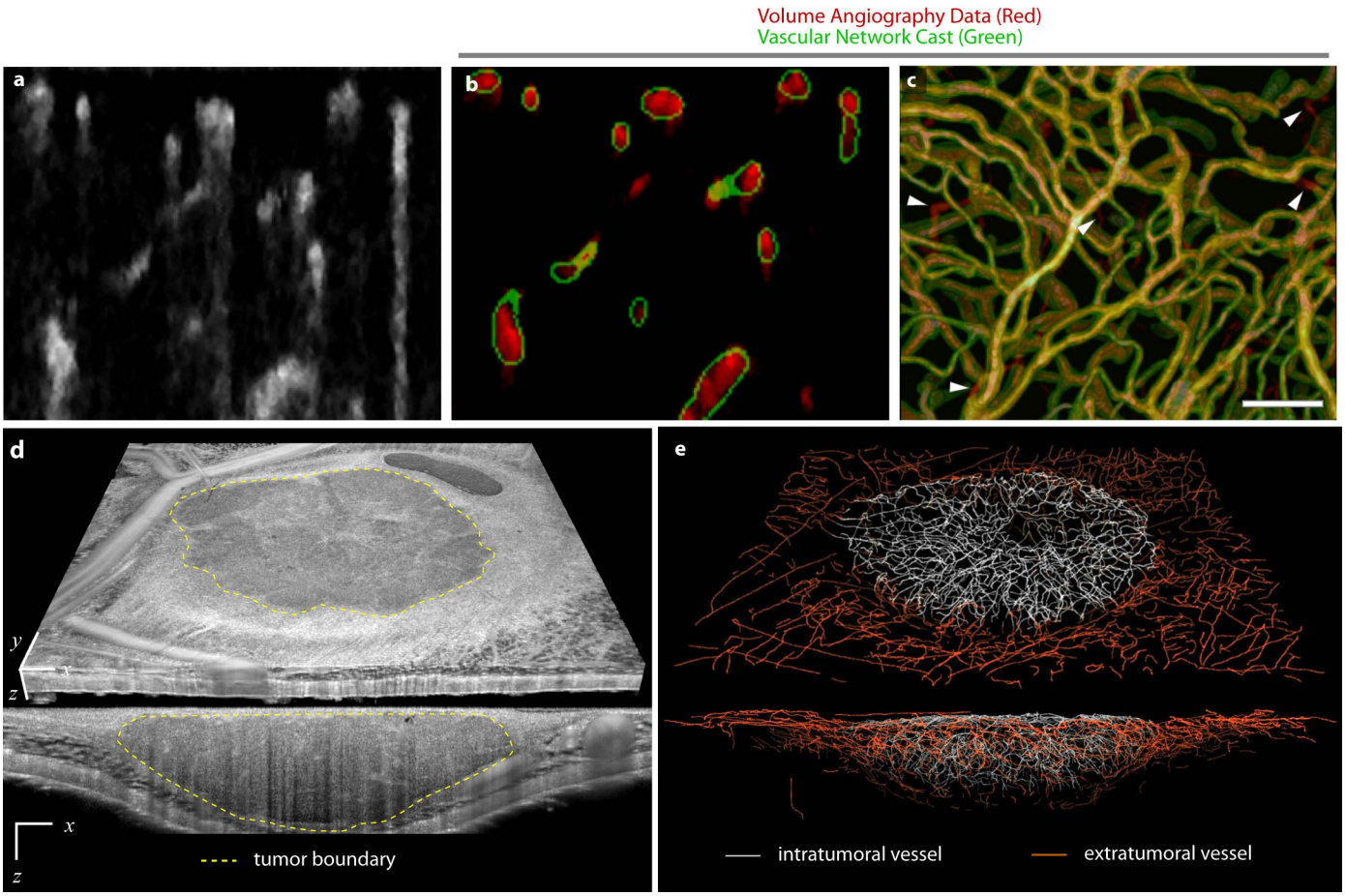

Supplementary Figure 6. Vascular tracing and structural correlation. (**a**) Cross-sectional OFDI angiographic data showing vessels and shadow artifacts extending below the vessels. (**b**) Dataset showing bitmap data (red) after shadow removal and vascular tracing contours (green). (**c**) Merged enface image of the vascular dataset (red) and a cast of the traced vessels (green) illustrating the inclusion of all but a few vessels (white arrowhead, ▻) within the cast. Scale Bar, 250 μm. (**d**) Microanatomical display showing tumor boundary definition in a three-dimensional tissue volume. (**e**) Skeletonized traced vessels differentiated between intratumoral and extratumoral for the tumor depicted in *d*. Transverse extent in *d,e*: 5 mm (x), 4.4 mm (y).

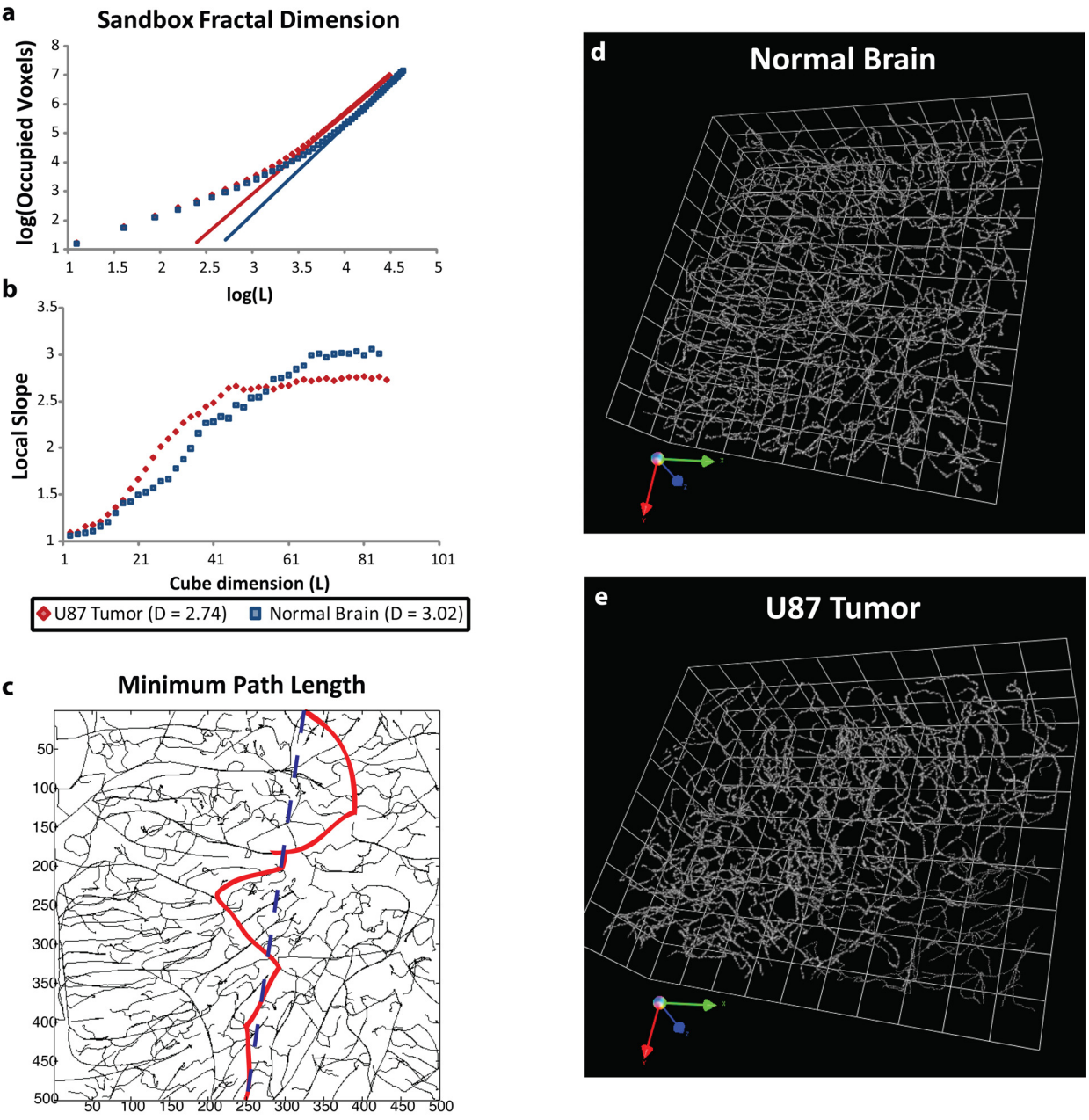

Supplementary Figure 7. Fractal characterization of tumor vascular networks imaged by OFDI angiography. (**a**) Representative example of the sandbox method for determining the fractal dimension of the vasculature of both normal mouse cortex and a human tumor glioblastoma multiforme (U87) tumor implanted in the mouse brain. A natural log of the mean number of occupied voxels within cubes of dimension (L) covering the three-dimensional network is plotted versus the natural log of the cube dimension. The slope of the linear portion of the plot determines the fractal dimension. (**b**) The local slope of the curves in *a* for each cube dimension. The fractal dimension is observed from the plateau regions corresponding to the linear portions in *a* (2.74 for the U87 tumor and 3.02 for normal brain). **c**, Depiction of the minimum path length for a given three-dimensional vascular network. Here, each path traversed from one face to the other is projected though the axial dimension with the minimum path length highlighted in red. The projection of the Pythagorean distance is shown as a dashed blue line. Tortuosity is determined from the ratio of these two distances. (**d,e**) The three-dimensional skeletonized vascular networks geometrically characterized in *a* and *b*. Each gridline is 250 μm.

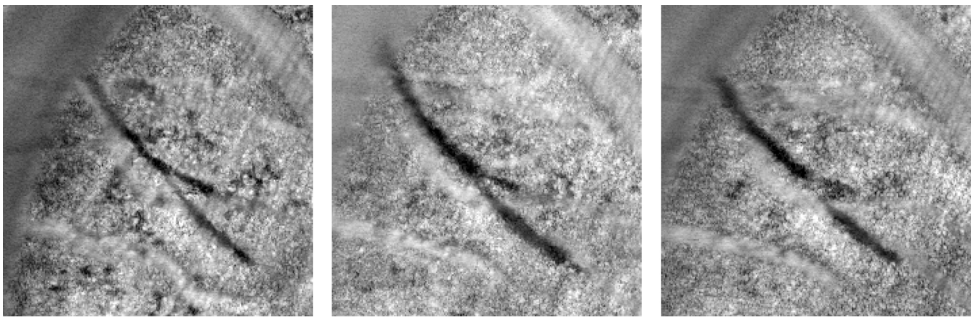

Supplementary Figure 8. Longitudinal tracking of lymphatics using OFDI. Changes in lymphatic vessel diameters are evident over 4 d during tumor (MCaIV) progression.

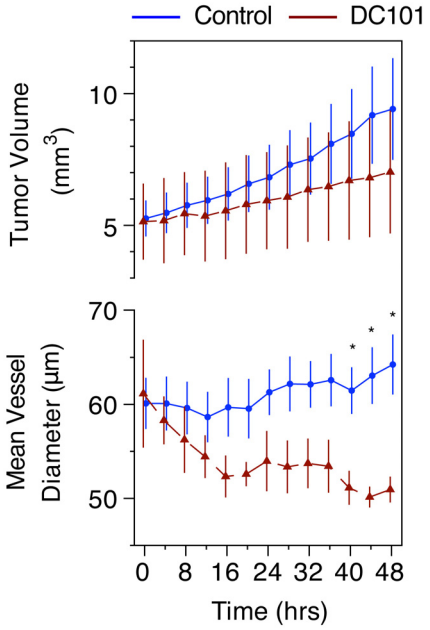

Supplementary Figure 9. Vascular dynamics of fields and time intervals not accessible with traditional approaches. Angiography at a 4 h interval over 48 h reveals the rapid response in vascular parameters to VEGFR-2 blockade. Vascular tracing registered to three-dimensional tumor boundaries allows quantification of the vascular changes within the tumor mass, showing nearly immediate changes to vascular diameter (*bottom*). The tumor growth rate of the treated group trends slower than control tumors, but is not significant over 48 h. (*top*). Control: n=4, DC101 n=3.

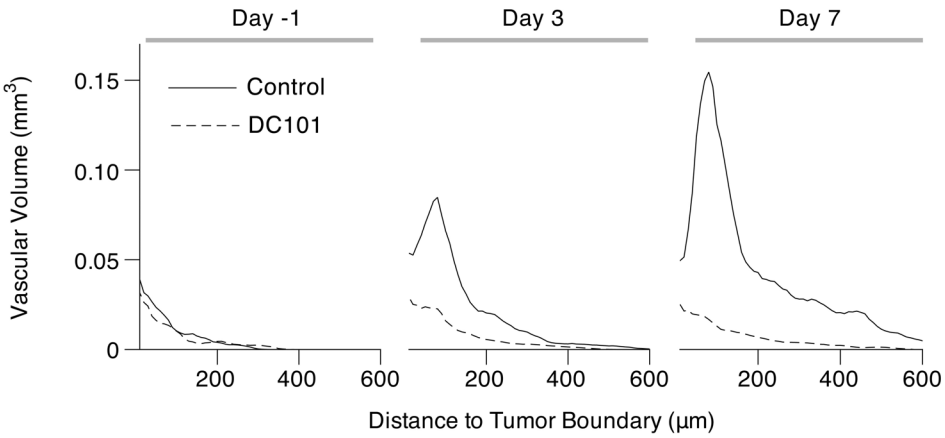

Supplementary Figure 10. DC101 treatment restrains intratumoral vascular growth near tumor margin. The mean vascular volume spatially correlated with the tumor boundaries across all animals reveals a region of specific increase within 200 μm of the tumor margin in control animals that is restricted in animals treated by anti-angiogenic therapy. (Control *n*=5, Treated *n*=6).

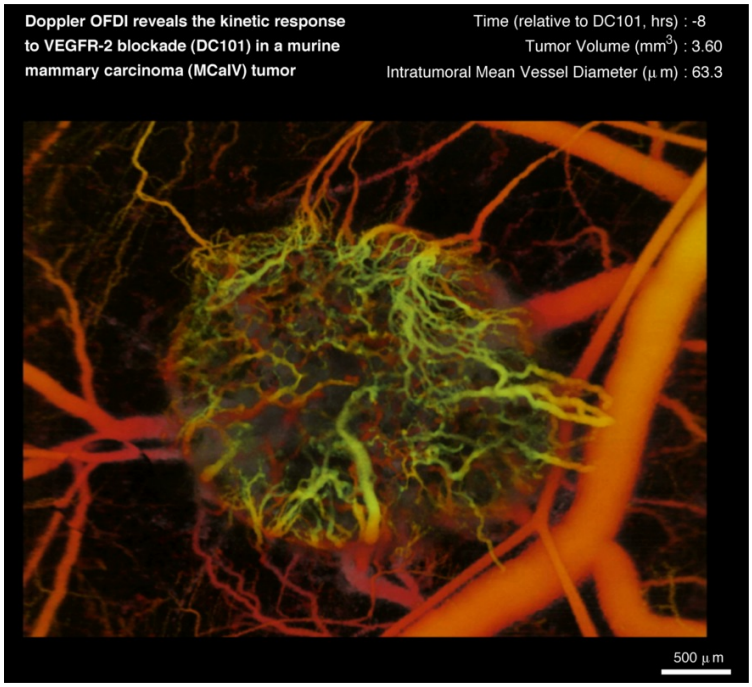

Supplementary Video 1. Time-lapse video of an MCaIV tumor implanted in the dorsal skinfold chamber. Changes in tumor microvasculature are shown starting 8 h before to 40 h after DC101 treatment. Tumor volume and mean intratumoral vessel diameter are tracked at 2 h intervals for 48 h.

Supplementary Methods on OFDI Signal Acquisition, Processing, and Quantification.

OFDI system and data acquisition. OFDI provides high resolution imaging of the elastic light scattering properties of a sample in three dimensions[1]. Beam focusing provides transverse (*x*,*y*) discrimination of signals. Interferometric measurements of optical delay gate signals across the axial (*z*) dimension. The measurements first sample in parallel the interference signal between light scattered at all detectable depths and an external reference beam as a function of wavelength. Subsequent Fourier analysis of this interference signal across wavelength separates the combined signals across all depths into a depth-resolved scattering profile. To measure interference signals across wavelength, a wavelength-swept laser source with an instantaneous narrow linewidth (<0.17 nm) is used (**Supplementary Fig. 1**). This laser source used a semiconductor optical amplifier (Covega Corp.) as a broadband gain medium in combination with a polygon scanner as a scanned wavelength filter (Lincoln Laser Corp.). Wavelengths sampled continuously a 140 nm window centered at 1300 nm, resulting in a depth resolution of 6 mm in tissue. Depth scans (A-lines) were acquired at a rate of 50 kHz. Through inclusion of an acousto-optic frequency shifter (Brimrose Corp.), a 5.8 mm scan range was achieved[2]. A polarization diverse optical demodulator generated an optical interference signal for each of two orthogonal polarization states, preventing artifacts due to polarization signal fading. The interference signals were digitized using a two-channel 100 MHz acquisition board (Signatec, Inc.), and were continuously archived to a high-speed hard-drive storage array. Real-time display of structural and vascular images at approximately 10% of the acquisition rate allowed monitoring of the imaging sessions and interactive definition of the imaging field. Transverse sampling patterns were developed to achieve rapid scanning across large volumes while simultaneously matching the Doppler detection range to the empirically determined optimal motion sensitivity. Data was acquired along the x-dimension at either a 5.0 μm pitch across a transverse field of 5.0 mm or a 7.62 μm pitch across a 7.8 mm transverse field, both at 16.3 frames per second. Each frame comprised 3072 A-lines that were combined in post-processing to provide 1024 structural and Doppler image lines. Data was collected in the y-dimension at a 0.56 μm pitch naively, and integrated in post-processing to yield a reduced dataset with isotropic sampling in the x-y dimensions of 5.0 μm/7.62 μm. Scanning along the y-dimension utilized physical translation of the animal at 9 μm/sec. The scanned field along this dimension was limited only by the chamber window aperture. Data along the depth dimension was acquired natively at a 4.1 μm pitch (in tissue) and signal was acquired over the first 1.5 mm to 2.5 mm in tissue, depending on scattering levels.

OFDI Signal and Image Processing and Quantification. Processed images and quantitative data describing microanatomy, blood and lymphatic vascular networks, and tissue viability in tumors were derived from a single raw data format using a series of core processing routines followed by parameter specific algorithms. These methods and algorithms are described here and summarized in a flowchart format (**Supplementary Fig. 2**).

Core Processing Routines. The OFDI system described in the methods recorded the interference signal across wavelength (λ) between a reference beam and an optical probe beam directed at a particular transverse locations of the sample (*x*,*y*) and at a particular timepoints (*t*). From this raw data, the optical scattering (complex parameter including amplitude and phase) as a function of (*x*,*y*,*z*,*t*) was generated as described above. This data was spaced at either a 5 μm or 7.62 μm pitch in the x dimension and at a 0.56 μm pitch in the y dimension. The same locations were resampled at 9 ms time intervals. This dataset described the scattering properties of a specific spatial location at multiple timepoints. From the complex scattering dataset, a set of three further datasets were derived that highlight specific properties of the scattering signal and formed the basis for subsequent processing (custom code written in programming language *c*). These datasets are described as follows:

(i) Microarchitecture: The magnitude of the scattering signals were averaged across time and the y-dimension to produce a time-independent three-dimensional magnitude scattering dataset with isotropic pitch in the (x,y) dimensions. This dataset was saved in log-scale to an 8-bit file (**microarch.tif**). *This dataset was used to reveal the microarchitectural features of the tissue.*

(ii) Phase Variation: The scattering signals at the sample transverse locations were compared across time to produce phase differences from (-π,π) at the native spatial pitch (5.0/7.62 μm x 0.56 μm x 4.1 μm). Each phase difference was weighted by the magnitude of the average signal from that point. The circular variances (from 0 to 1) of these amplitude-weighted phase-difference datasets over 50 μm depth windows were calculated at each point in three-dimensional space. A three-dimensional angiographic dataset was then obtained by combining (median) appropriate sample counts in the y-dimension to yield isotropic pitch in the transverse dimensions. The data was saved to an 8-bit dataset (**phasevar.tif**). The use of the amplitude-weighted circular variance over this limited depth window both minimized phase decorrelation and optical noise artifacts by amplitude weighting the phase-

differences and reduced artifacts due to background motion resulting from respiration, muscular contractions, and environmental instabilities. *This dataset was used to reveal the vascular regions in the tissue.*

(iii) Phase Variation Weight: The magnitude of the scattered signals that were used to derive the phase variation signal was calculated at the native spatial pitch, and then combined in the y-dimension (mean) to yield isotropic pitch in the transverse dimensions. The data was saved to an 8-bit dataset (**phaseweight.tif**). *This dataset was used to weight the phase variation signal and discriminate between vascular regions and low-signal regions.*

These datasets formed the basis for further analysis yielding images and quantitative data for specific biological parameters as is described in the following sections. Unless otherwise noted, the parameter specific processing was performed in Matlab (The Mathworks, Natick, MA).

Three-Dimensional Tumor Volume and Boundary Calculation. For tumor volume calculations, an *en face* projected image was calculated by averaging the signals from 160 μm to 240 μm in depth from the microarchitectural dataset (**microarch.tif**). The location of the tumor center in (x,y) was recorded manually from this image. Using this location and the microarchitectural dataset (**microarch.tif**), a series of 8 cross-sectional images was generated through the tumor center at equally spaced angular increments, i.e., along the meridian planes through the tumor center defined by 0/180°, 22.5/202.5°, 45/225°, 67.5/247°, 90/270°, 112.5/292.5°, 135/315°, and 157.5/337.5°. To improve contrast in these images, the scattering signal was integrated over 80 μm in the transverse dimension perpendicular to the plane of each cross-sectional image. The tumor boundaries were manually segmented in these images using ImageJ (ImageJ 1.39, open source NIH software, http://rsb.info.nih.gov/ij/index.html). From the tumor boundaries in the 8 meridian planes, the tumor boundaries in three-dimensional Cartesian space were calculated by interpolation yielding a tumor mask defining the intratumoral volume and extratumoral volume within the three datasets (**microarch.tif**, **phasevar.tif**, **phaseweight.tif**). The tumor volume was calculated from this mask and the known pitch of these datasets.

Normalized Scattering/Viability. The mean scattering intensity within tumors grown in window models was derived from the set of 8 cross-sectional images after normalizing for scattering intensity across depth. In these eight cross-sectional images, the location of the backside Dermis was identified using ImageJ. The scattering signal intensity of this layer was used to derive the average scattering attenuation with depth for every depth scan within each cross-sectional image. Normalized cross-sectional images were generated by applying a uniform signal gain across depth that compensated the derived attenuation. From these normalized cross-sectional images and the tumor mask, the average scattering within the tumor volume was calculated.

Quantification of Viable Fraction. To assess the viable fraction, depth-matched 20-40 μm *en face* projections of both the phase variation (**phasevar.tif**) and microarchitectural (**microarch.tif**) datasets were manually selected. The tumor margins were manually identified from the scattering differences in the microarchitectural dataset and a mask was created to restrict further analysis to the tumor region. Using the phase variation dataset, the vascular signal was identified by thresholding the image to create a binary mask highlighting the vascular network. A vascular distance map (distance of each pixel in the intravascular space to the nearest vessel) was then determined using a 2-dimensional Euclidean distance transform in Matlab. The mean scattering index for distances from 0-1000 μm were determined using the distance map and the pixel values in the microarchitectural datasets. Plots of mean scattering index versus distance from nearest vessel revealed sigmoid shaped curves. For each timepoint, the scattering index at the inflection point was selected as the threshold value to differentiate viable from non-viable tissue in the microarchitectural dataset and determine the area in pixels of each region in the intravascular space. For each timepoint, the tissue fractions of vascular, viable, and necrotic/apoptotic regions were then determined from the area in pixels of each over the total pixel area of the tumor. Additionally, the mean distance of each pixel region (viable or necrotic/apoptotic) to the nearest vessel was determined using the distance map and thresholded pixels from the microarchitectural dataset. To visually illustrate the different regions of viable tissue in the tumor, a colormap was selected and adjusted so that the threshold scattering index for each timepoint was indexed to the green region of the colormap (blue/light blue indicating viable and yellow/red indicating non-viable).

Quantitative Lymphangiography. Lymphatic vessels are identified through the diminished scattering signal within the microarchitectural dataset (**microarch.tif**) from the intraluminal lymph, likely attributed to hypocellularity and lower protein concentration. The distinct network topology and vessel characteristics coupled with the correspondence of these ascattering structures with Evan's blue lymphangiography (**Fig. 3**) confirm their identification as lymphatic vessels. Presentations of the lymphatic networks were generated by manual selection of the lymphatic bed depth within

the microarchitectural dataset (**microarch.tif**) at a series of transverse locations. A curved but continuous depth plane through the lymphatic bed was defined by first interpolating the location of the lymphatic bed across all transverse points using three-dimensional cubic interpolation through Delaunay triangulation, and then smoothing this curve through application of a two-dimensional Gaussian filter of kernel size of 250 μm. Minimum intensity projections across depth over regions within +/-50 μm of the lymphatic bed were then generated to reveal the network in a two-dimensional image (**Fig. 3**). The maximum diameter of lymphangions (lymphatic vessel segment) were measured in the XY plane with ImageJ software. Monitoring of lymphatic vessels over time (**Supplementary Fig. 8)** used microarchitectural, vascular, and lymphatic features as landmarks for co-registration across timepoints.

Quantitative Angiography. Vascular quantification was performed through automated vessel tracing. To condition the vascular dataset for tracing, the following steps were performed:

(i) If necessary, a mask file was generated manually (ImageJ) that delineates the vascular signatures in the phase variation dataset (**phasevar.tif**) from artifacts associated with low-signal intensities in the air or Brownian motion in the fluid above the non-planar tissue surface.

(ii) Doppler techniques suffer from artifacts due to forward scattering of red blood cells that result in signal shadows extending below the deepest extent of a vessel. For large vessels with high local hematocrit, shadowing can extend to nearly all of the lower depths. These artifacts frustrate the automated three-dimensional analysis of vascular networks. To reduce this shadowing, we further processed the angiographic datasets by applying a step down exponential filter. Working from the surface of the tissue downward, the magnitudes of the vascular signal (**phasevar.tif**) of all points below the current point were attenuated according to the magnitude of the current point. A deshadowed dataset (**phasevar_noshadow.tif**) was generated as the output. A result of this technique is that small vessels underneath very large vessels were obscured and not traced.

After shadow removal, an automated three-dimensional vessel tracing algorithm was applied to the deshadowed datasets (**phasevar_noshadow.tif**, **Supplementary Fig. 6**). The tracing algorithm was developed and adapted for the OFDI images from a model previously applied to angiographic images from multiphoton microscopy[3]. Briefly, the model traverses the vascular network with cylindroidal superellipsoids fit to the vessel boundaries by minimizing region-based statistics using a likelihood ratio test to differentiate between noise and other artifacts. In addition to providing the three-dimensional geometry of vessels segmented by the superellipsoids, the model defines vessel centerlines, intersections, and branches. Novel seeding algorithms were developed for the OFDI datasets to provide robust initial guesses for vascular regions without the requirement of segmentation procedures.

Prior to commencement of the vascular tracing algorithm, homomorphic filtering was applied to each deshadowed phase variation dataset. Homomorphic filtering consisted of first convolving a low-pass Gaussian filter across each transverse (XY) slice of the deshadowed datasets to lower the background signal. The intensity in the resultant image was then homogenized at both the low and high ends of the intensity spectrum to increase contrast. To remove any remaining specular noise resulting from the filtering process, a median filter was applied to each transverse slice of the three-dimensional OFDI dataset.

For each superellipsoid describing a "vascular segment", the parameters output from the tracing algorithm provided a centroid, major, minor and longitudinal axes and quaternary rotation parameters defining the rotation of the axes from image space to fitting space. Vessels were defined by the fitting algorithm as a series of vascular segments between intersections, branching points or dead ends. The model fit to each vascular segment was performed in unitary space rotated from the actual image space so that all superellipsoid axes rested on the axes defining Cartesian coordinates of this space. To obtain quantitative measures in image space, the superellipsoid axes were rotated back into image space and the magnitudes in microns of each axis were determined by the pixel dimensions in three-dimensional space.

Due to the shadow removal processing, vessel morphology in the xz or yz planes were altered in some cases. Therefore, morphological measurements were always made as projections onto the xy plane. The two shortest superellipsoid axes were used for the projection onto the xy plane. To determine the length of each vascular segment, the distances between adjacent centroids (as defined by the tracing algorithm) were determined. Vascular diameter for a given set of segments (i.e. intratumoral) was determined by weighting the xy-projected diameter for each segment by its length. Vascular length of a given volume of tissue was simply the sum of the length of all vascular segments in that region. Vascular

volume was determined by calculating the area containing the segment centroid and then multiplying by the segment length and summing over all segments of interest.

To assess intratumoral spatial differences in morphological responses of the vasculature, selected parameters were analyzed according to their three-dimensional distance to the tumor boundary defined by the aforementioned techniques. For example, the mean vascular volume in the control group of the DC101 experiment presented in Fig. 5 that was within 200 μm of the margin was found to dramatically increase with tumor growth. Comparatively, DC101 treatment restrained vascular volume in this region (**Supplementary Fig. 10**).

Three-dimensional image casts or skeletons of the vascular networks were obtained from the parameters output by the vascular tracing algorithm using Matlab. Visualization was obtained using either Volocity (Improvision, Inc) or OsiriX (The OsiriX Foundation, Open-Source Software).

Fractal statistics describe properties of the vascular network that are distinct from those described by conventional metrics such as vessel density. The fractal dimension characterizes the degree of space-filling and self-similarity of a vascular network without accounting for the diameter or number of individual vessels. The tortuosity is only a measure of the shortest connectivity in a network and is independent of vascular density. The fractal dimension was calculated using the sandbox method[4] adjusted for the voxel size anisotropy in three-dimensions. Skeletonized vascular networks were obtained using the vessel parameters defined by the vascular tracing algorithm. A three-dimensional rectangular region of the image volume was selected for geometrical analysis. For analysis of tumor vascular networks, the rectangular region of largest size was selected that was within the tumor boundary. A point near the center of the structure was randomly selected and surrounded by cubes of increasing dimension through multiple iterations. The mean number of occupied voxels within each cube of a particular length scale was determined by averaging over all selected voxels. The linear slope of the log-log plot of mean occupied voxels versus cube dimension defined the fractal dimension (**Supplementary Fig. 7**). A complementary metric to fractal dimension is the tortuosity, defined as the ratio of the minimum vascular path between two points and the geometric distance between those points. As the tortuosity parameter increases from its minimum value of 1.0, the transport efficiency of the vascular network decreases. The minimum path length was found by determining the minimum length between occupied voxels on each pair of opposite faces in the skeletonized vascular network defined above. Tortuosity was calculated by taking the ratio of the minimum path length to the Pythagorean distance measured between the first and last point of the path.

Visualization. The generation of combined blood and lymphatic vascular projections required segmentation of the lymphatic networks from the surrounding tissue. The lymphatic networks were semi-automatically segmented by the manual selection of points within lymphangions followed by the expansion of these points using a three-dimensional region growing algorithm. The resulting segmented lymphatic network described the interluminal volume of the identified lymphatic vessels in three-dimensional space registered to the vascular dataset (**phasevar.tif**).

Reduction of the three-dimensional vascular (blood and/or lymph) datasets to a single *en face* image utilized a customized volume up rendering technique. The vascular dataset (**phasevar.tif**) was three-dimensional median filtered with a kernel size of (3x3x3). The blood vessel signals in this filtered dataset were then colorized according to their depth. Within the segmented lymphatic network image, lymph vessels were colored blue. These datasets were then merged if rendering both blood and lymph vessels. Finally, the vascular (blood) or merged (blood and lymph) dataset were reduced to an *en face* presentation using volume up rendering techniques[5] wherein each pixel is assigned an opacity and more superficial features are layered over deeper structures. The opacity of each pixel was calculated as a product of the vascular signal magnitude (**phasevar.tif**) and the signal weight of that vascular signal (**phasevarweight.tif)**.

Multiphoton microscopy and registration. Multiphoton imaging was performed with a custom-modified confocal laser scanning microscope (Olympus 300; Optical Analysis Corp.) using a broadband femtosecond source (High Performance MaiTai, SpectraPhysics). Angiographic contrast was achieved through intravenous administration of 200 μl of 8 mg/ml fluorescein isothiocyanate dextran 2M molecular weight (FITC-Dex 2M, Sigma-Aldrich) in phosphate buffered saline. Image stacks were taken at 800nm excitation (~60 mW at sample surface) with depths ranging to 500 μm depending on animal model and tumor type. To image tumors or organs (brain) over wide-fields, collections of mosaic images were taken in raster pattern using a motorized stage (H101, Prior Scientific, Inc.) and customized automation software (LabView, National Instruments). Mosaic stacks were assembled using ImageJ (NIH, Bethesda, MD) and Matlab (MathWorks). Registration between MPM and OFDI of the same sample was conducted by denoting imaging regions on the window coverglass by histological markers and manually

comparing the locations of large vessels. All multiphoton imaging studies were performed with a 20X magnification, 0.95NA water immersion objective (Olympus XLUMPlanFl, 1-UB965, Optical Anaylsis) with estimated $\frac{1}{e^2}$ radii of 0.27 μm radially and 1.14 μm axially.

1. Yun, S.H., Tearney, G.J., de Boer, J.F., Iftimia, N. & Bouma, B.E. High-speed optical frequency-domain imaging. *Opt. Express* **11**, 2953-2963 (2003).
2. Yun, S.H., Tearney, G.J., de Boer, J.F. & Bouma, B.E. Removing the depth-degeneracy in optical frequency domain imaging with frequency shifting. *Opt. Express* **12**, 4822-4828 (2004).
3. Tyrrell, J.A*., et al.* Robust 3-D modeling of vasculature imagery using superellipsoids. *IEEE Trans. Med. Imaging* **26**, 223-237 (2007).
4. Gazit, Y*., et al.* Fractal characteristics of tumor vascular architecture during tumor growth and regression. *Microcirculation* **4**, 395-402 (1997).
5. Levoy, M. Display of surfaces from volume data. *Computer Graphics and Applications, IEEE* **8**, 29-37 (1988).